A novel transplantable model of lung cancer associated tissue loss and disrupted muscle regeneration

Paige C Arneson[1+], Alexandra M Ducharme[1+], Jason D Doles[1*]

[1]Department of Biochemistry and Molecular Biology, Mayo Clinic, Rochester, Minnesota, 55905 USA, Mayo Clinic, Rochester, Minnesota.

[+]These authors contributed equally to this work

*Corresponding author and lead contact

DESCRIPTIVE ABSTRACT

Background: Cancer-associated muscle wasting (CAW), a symptom of cancer cachexia, is associated with approximately 20% of lung cancer deaths, and remains poorly characterized on a mechanistic level. Current animal models for lung cancer-associated cachexia are limited in that they: 1) primarily employ flank transplantation methods, 2) have short survival times not reflective of the patient condition, and 3) are typically performed in young mice not representative of mean patient age. This study investigates a new model for lung cancer-associated cachexia that can address these issues and also implicates muscle regeneration as a contributor to CAW.

Methods: We used tail vein injection as a method to introduce tumor cells that seed primarily in the lungs of mice. Body composition of tumor bearing mice was longitudinally tracked using magnetic resonance imaging (MRI). These data were combined with histological and molecular assessments of skeletal muscle to provide a complete analysis of muscle wasting.

Results: In this new lung CAW model we observed 1) progressive loss in whole body weight, 2) progressive loss of lean and fat mass, 3) a circulating cytokine/inflammatory profile similar to that seen in other models of CAW, 4) histological changes associated with muscle wasting, and 5) molecular changes in muscle that implicate suppression of muscle repair/regeneration. Finally, we show that survival can be extended without lessening CAW by titrating injected cell number.

Conclusions: Overall, this study describes a new model of CAW that could be useful for further studies of lung cancer-associated wasting and accompanying changes in the regenerative capacity of muscle. Additionally, this model addresses many recent concerns with existing models such as immunocompetence, location of tumor, and survival time.

INTRODUCTION

Cancer cachexia is a complex syndrome associated with approximately 20% of lung cancer deaths; a hallmark symptom of cancer cachexia is cancer-associated muscle wasting (CAW) [1, 2]. Although this syndrome is associated with negative patient outcomes, it remains poorly understood on a mechanistic level. Many groups have investigated the inflammatory environment associated with CAW, in particular, inflammatory cytokines such as tumor necrosis factor alpha (TNFα) and interleukin 6 (IL6). Despite considerable time invested in this area, clinical trials targeting the inflammatory microenvironment alone have been unsuccessful [3, 4]. Other groups have focused on the proteolytic environment in muscle, as a potential driver of CAW, implicating both autophagy and ubiquitin-mediated pathways as potential drivers of CAW [5-7]. The current mechanistic understanding of CAW is largely based off of work done in mouse models, most notably the Lewis lung carcinoma (LLC) and C-26 models.

The LLC model of CAW relies on transplantation of LLC1 non-small cell lung cancer cells, derived from C57/B6 mice, into syngeneic, and thus immunocompetent, C57/B6 recipient mice. The LLC model is one of the few syngeneic and reproducible models for lung cancer/lung-cancer associated wasting available today [8]. Most commonly, LLC1 cells are implanted via flank injection, which results in large primary tumors around 7 days post implantation. A second popular model for CAW, the C26 model, was first described in 1990 and utilizes flank injection of colon 26 carcinoma cells [9]. Like the LLC model, this model displays elevated expression of proteasome components, which contribute to loss of muscle mass [10]. The C26 model presents with longer median survival (25 days) than the LLC model [10]. Notably, both the C26 and LLC models share a common weakness in that tumors do not arise in the tumor tissue of origin. Although recent studies have attempted to correct this issue using autochthonous genetically engineered mouse models (GEMMS), their utility and flexibility are limited. For example, in pancreatic cancer, there have been multiple efforts to create CAW models that focus on tumors arising in their

native tissue via either genetic manipulation or orthotopic implantation [11-15]. The benefits and limitations of these models are addressed in more depth in the discussion. Despite these advances in the context of pancreas cancer, lung cancer models have lagged behind. Orthotopic transplantation has been established in rodent models, but requires an invasive surgery [16] [17]. Furthermore, genetic methods to derive orthotopic tumors in lungs require viral delivery of Cre recombinase [18]. Complications arising in both these models are high and prompted us to develop a simple, reproducible, and scalable model of lung CAW.

We identified the need for better models of CAW that met the following criteria: 1) immunocompetent environment, 2) tumors arising in the appropriate/matching tissue of origin, and 3) ability to modulate the timing/duration of wasting. Here, we present studies on a novel mouse model for lung CAW, which has met these criteria. This model utilizes syngeneic, immunocompetent mice and tail-vein injection of cells as a modality for lung tumor seeding; shows a median survival of approximately 26 days that can be modulated as a function of injected cell number; and exhibits hallmarks of lung CAW. The model presented herein fills a gap in models for studying CAW, and will be a valuable resource for the wasting community moving forward.

RESULTS

Development of a transplantable model for lung cancer-associated tissue loss

Given the increasing need in the CAW field for models featuring tumors arising in their natural location, we sought to develop such a model in the context of lung cancer. To accomplish this, we used tail vein injection as a method whereby injected lung tumor cells implant primarily in the lungs [19]. Cells were derived from a murine lung adenocarcinoma and cultured more than 10 passages prior to injection. Cells were suspended in PBS for the injection and control animals were injected with PBS vehicle only. Throughout the course of the study we assessed body composition via magnetic resonance imaging (MRI) until humane endpoint (see experimental schematic in **Figure 1A**). We performed survival studies on 3 cohorts of mice (total n=10 vehicle and 15 tumor) and observed significantly decreased survival for tumor bearing mice (average survival tumor=26.2 days) (**Figure 1B**). Upon macroscopic inspection of the lungs, tumor bearing mice had many small nodules, fibrotic tissue, and increased tissue density (**Figure 1C**). Upon microscopic inspection of the lungs in tumor-bearing mice, alveolar fields were replaced by multiple, coalescing tumor nodules (>70% in 3 animals, 40-50% in 2 animals assessed). The tumor nodules consisted of loosely packed, vacuolated cells and in some cases were associated with small clusters of intra-tumoral lymphocytes, usually at the margins of blood vessels or nodules. Lastly, the pleural surface was roughened by projecting fronds / plaques of tumor cells. In comparison, vehicle animals displayed expanded alveolar spaces and a smooth pleural surface (**Figure 1D**). Furthermore, we observed a statistically significant increase in total lung weight in tumor-bearing mice (**Figure 1E**).

Concurrent with evaluations of tumor effects on overall survival, we performed longitudinal body composition analyses. First, we observed a significant difference in time and treatment co-variance for body weight, which was highlighted by significant decreases in body weight at 10, 14, and 17 days post tumor implantation (**Figure 1F**). Next, we observed a significant difference in time and treatment co-variance for total fat mass, which was highlighted by significant

decreases in fat mass at 14, 17, and 21 days post tumor implantation (**Figure 1G**). Lastly, we observed a significant difference in time and group co-variance in total lean mass, although individual days had no significant difference (**Figure 1H**). Overall, there were decreases in total body weight, total fat mass, and total lean mass as the tumor progressed (the latter two measured by MRI) (**Figure 1F-H**).

Lung cancer-associated inflammation

Loss in both body weight and lean mass are hallmarks of CAW. Many studies have implicated heightened inflammatory signaling as a driver of CAW [20-22]. We quantitatively assessed concentrations of 31 cytokines in the serum of tumor-bearing and vehicle animals (EveTechnologies) (n=5 vehicle and 4 tumor). Ranked analysis (vertically by their average in the tumor-bearing animals; highest to lowest) revealed substantial differences between experimental groups (**Figure 2A).** Specifically, we observed significant differences in 4 factors: Eotaxin (down~2 fold), C-X-C motif chemokine 5 (LIX, down ~10 fold), TNFα (up ~30 fold) and vascular endothelial growth factor (VEGF, up ~190 fold) (**Figure 2C**). Of note, TNFα accumulation has been previously implicated in CAW [20, 23].

Lung cancer-associated muscle loss

Considering both the loss of lean mass by MRI analysis and the accumulation of classical markers of CAW in the serum, we next performed a histological and molecular assessment of skeletal muscle. First, we assessed tibialis anterior (TA) muscle cross sections by immunofluorescent staining for laminin, a marker of myofiber membranes, and DAPI (nuclei) (**Figure 3A**). Minimum feret diameters were measured, compiled, and calculated using myovision (mean feret diameter: 3 million = 40.4 um, vehicle = 44.4 um, and found a statistically significant decrease in the non-linear regressions fit to the histograms of minimum feret diameter distribution of tumor-bearing mice(**Figure 3B**) [24]. Additionally, we observed a significant decrease in TA weight in tumor bearing animals; this was not due to a reduction in the total number of myofibers in the TA of these animals

(**Figure 3C-D**). Since we observed a reduction in myofiber size, but not total number of myofibers, we postulated that this could be due to a decrease in the regenerative capacity of muscle. Using immunofluorescent staining, we queried the number of Pax7 positive muscle progenitor cells. We observed a statistically significant increase in Pax7 positive cells per millimeter squared of tissue (**Figure 3E**). Additionally, we assessed the number of centrally located nuclei (CLN), which mark actively regenerating myofibers containing recently fused muscle progenitor cells. We did not see any difference in the number of CLN per millimeter squared of tissue between vehicle and tumor-bearing mice (**Figure 3F**). Lastly, to acquire a molecular understanding of regenerative capacity of muscle from tumor-bearing animals, we used quantitative RT-PCR to measure several transcripts associated with early myogenesis, late myogenesis/fusion, and muscle atrophy. Visualized in a heat map, we see a trend toward higher expression of atrophy transcripts (Trim63 and Fbxo32) and early makers of myogenesis (Pax7 and Myod1), and lower expression of late markers of myogenesis (**Figure 3G**).

Transplanted cell number correlates with survival and CAW progression

Upon establishing that our lung cancer model induces loss in total body weight, lean mass, and is also associated with an impaired muscle regeneration phenotype, we sought to determine if survival time/CAW progression could be experimentally modulated. To accomplish this, we varied the number of cells injected as follows: 3 million cells (used in all previous figures), 1 million cells, 300,000 cells, and vehicle. We also tested 30,000 and 3,000 cells but found inconsistent inoculation of tumors and omitted these groups from further study (data not shown). We assessed survival of animals in each group and found that lowering the number of cells injected prolonged survival as evidenced by a statistical increase in survival from 3 million to 1 million cells ($p=0.0208$), 1 million to 300,000 cells ($p=0.0024$), and 300,000 cells to vehicle ($p=0.0046$) (**Figure 4A-B)**. We also observed changes in lung condition, as evidenced by increased lung weight in 3 and 1 million injected cells, and macroscopic changes in lung condition similar to those observed previously (**Figure 4C-D**).

We next performed body composition and muscle morphometrics analyses in mice receiving variable numbers of tumor cells. As before, we observed decreasing trends in body mass, lean mass and fat mass in tumor bearing mice of all groups (**Figure 5A-C**). Specifically, we observed significant difference in time and treatment co-variance for body weight, in 3 million, 1 million, and 300,000 implanted cell groups compared to vehicle (**Figure 5A**). We also observed significant difference in time and treatment co-variance for total lean mass in 3 million and 1 million implanted cell groups compared to vehicle (**Figure 5B**). In lower implantation doses, we did not observe significant differences in total fat mass. Because tumors were restricted primarily to the lungs (with the exception of some metastases) (**Table 1**), it was not possible to discount tumor mass from MRI measurements. Evaluation of TA muscles from tumor-bearing mice revealed statistically decreases in TA mass in the 300,000 cells group, similar to the 3 million cells group (**Figure 5D**). Additionally, myovision-based assessment of minimum feret diameters revealed increasingly significant decreases as the cell injection number decreased (mean feret diameter: 1 million = 41.3 um, 300,000 = 32.6 um, vehicle = 44.4 um)(**Figure 5E**).

DISCUSSION

In order to gain a more thorough understanding of CAW, there is a need for models that more accurately capture the patient condition. This new and novel model for CAW meets several needs in the field such as: 1) immunocompetence (i.e. a syngeneic model), 2) exhibits both heightened catabolism and suppressed regeneration 3) exhibits both lean and fat mass loss, 4) exhibits an inflammatory microenvironment, 5) is flexible in timing and severity, 6) arises in the tumor's organ of origin. To the last point, recent studies have highlighted the importance of tumor location on both tumor development and CAW [25-27]. Our model is an easy and effective method to induce tumor formation in the lungs and concomitant CAW, using lung adenocarcinoma cells.

With regard to points two through four, developing therapeutics for CAW is ultimately dependent on mouse models that reflect the complex molecular nature of this syndrome. We showed that this model exhibits an inflammatory signature similar to published signatures of CAW patients [20, 21, 28-30]. Additionally, our model supports numerous studies linking both elevated catabolism and impaired skeletal muscle regeneration as contributors to CAW [5-7, 31]. Our observation that there is an accumulation of Pax7+ cells in the TA muscle, but no change in the number of centrally located nuclei may be indicative of increased progenitor cell expansion, with failure to incorporate into the damaged/cachectic muscle. Although we probed genes related to fusion and progenitor cell maturation by qPCR and did not observe differences in expression, a more detailed assessment of the progenitor cell population would be necessary to make definitive conclusions about suppressed muscle regeneration in this model.

A major weakness of many CAW mouse models is the age of wasting onset. Genetic models, such as the KPC model, are predisposed to spontaneously develop tumors, which gives investigators little control over the age of onset. With cachectic cancers affecting a primarily elderly population, it is critical that new models are able to account for this confounding factor. For pancreatic cancer, this problem has largely been solved by the KPP mouse, which

expresses pancreas-specific oncogenes under Cre recombinase control [13]. However, for lung cancer, this is only beginning to be addressed[15]. Although our model has not yet been adapted for use in aged mice, the transplantable nature of the model permits use in any age of animal. Our model has the added attraction that it does not require a major surgery or viral infection, which could affect inflammatory status, making it more amenable for aged animals with higher frailty than young animals [32].

The lack of CAW models that accurately assess the effects of age highlights a second issue, which is the difference between muscle atrophy and the absence of growth. A primary concern with the KPC pancreatic cancer mouse model is that these mice are significantly smaller than littermate controls prior to palpable tumor development. This suggests that fetal expression of the oncogenes is contributing to impaired muscle development [13]. Although spontaneous genetic models, such as the KPC model, are dramatic examples of the difference between atrophy and absence of growth, this principle implicates many transplantation models [33]. Even in the study presented here, with age-matched controls, it is evident that mice in the 3-6 month age group are still growing (gaining total body weight and fat mass). Although muscle development is typically considered complete at 3 months and lean mass is essentially stabilized in our animals, this anabolic state is unrepresentative of the patient population [13, 34, 35]. The model presented here is amenable to assessing CAW in aged animals (greater than one year), which may lead to a better understanding of CAW mechanisms and more efficient translatability to the clinic.

Another aspect of the patient condition poorly modeled in rodents is the severity and duration of wasting symptoms. Recently, it was established that the cachexia syndrome could be divided into three clinical stages: pre-cachexia, cachexia, and refractory cachexia. Although refractory cachexia is marked by a short (only three months) survival, wasting is present for much longer – an important observation that is difficult to study in rapidly progressing rodent CAW models. Importantly, with respect to intervention, some suggest that it is in the earlier stages (non-refractory) that therapeutics may be more effective [36]. Despite these features in

patients, mouse models like LLC and C26 have rapid symptom onset and short survival times. Failing to capture the earlier stages of cachexia is likely a contributor to the failed clinical trials based on pre-clinical data derived using these models. The ability of our model to be titrated by cell dosage provides an important opportunity explore the timing and duration of wasting symptoms more thoroughly.

Despite the many strengths highlighted in this study, the model presented herein does have limitations. Perhaps the most notable limitation is one common to all orthotopic lung cancer models, which is the difficulty for assessing tumor burden in living animals. This could be remediated by stably transfecting cells with a fluorescent reporter and utilizing *in vivo* imaging modalities. Additionally, in some cohorts, we observed high levels of metastasis outside the thoracic cavity. This may be representative of patients that exhibit metastases, but also complicates data interpretation. Nevertheless, the model presented here is an important step forward as CAW research progresses and will be a valuable resource for future research aimed at understanding the etiology of lung cancer-associated muscle and fat wasting.

ACKNOWLEDGEMENTS

The authors wish to thank members of the Doles lab for helpful discussions and manuscript suggestions. Additionally, the authors extend thanks to Brad Bolon, DVM, MS, PhD of GEMpath INC for assisting in the pathological analyses. J.D. was supported by the National Institute of Health/National Institute of Arthritis, Musculoskeletal and Skin Diseases (NIH/NIAMS) R00AR66696, Mayo Clinic start-up funds, Career Development Awards from the Mayo Clinic SPORE in Pancreatic Cancer (NIH/ National Cancer Institute (NCI) CA102701) and the American Association for Cancer Research/Pancreatic Cancer Action Network. P.C.A was supported by the Mayo Clinic Regenerative Sciences Training Program (RSTP).

AUTHOR CONTRIBUTIONS

Study design: JDD, PCA, AMD. Data collection: PCA and AMD. Data analysis/interpretation: JDD, PCA, AMD. Writing and editing of manuscript: JDD, PCA, AMD. All authors approved this manuscript.

COMPETING INTERESTS STATEMENT

The authors have no competing interests to declare.

FIGURE LEGENDS

Figure 1: Transplantable model for lung cancer-associated tissue loss. (A) Schematic of the study design. D0 = day tumor cells were injected into mice. All studies were survival studies, so endpoint was variable, but the median survival was 26 days. MRI scans were completed twice per week during the course of the study. **(B)** Survival curve for vehicle and tumor injected cells. Dotted vertical line indicates the median survival (26 days). N- 10 vehicle, 15 tumor. Data were compiled from 3 independent cohorts of animals. Survival is statistically different ($p<0.0001$) by Gehan-Breslow-Wilcoxon test. (**C)** Representative images of lungs from vehicle and tumor bearing mice. Ruler reference in centimeters. **(D)** Representative hematoxylin and eosin (H&E) staining of lung tissue from vehicle (left) and tumor bearing (right) mice. 2 representative images from 2 individual animals in each condition. Scale bar is 800 um. **(E)** Total lung weight (all lobes) from vehicle and tumor-bearing mice. Individual points represent individual animals. Boxes represent the inner quartiles and whiskers represent the minimum and maximum values. **(F)** Total mouse weight across study, normalized to pre-tumor baseline weight. Error bars are SEM. p values presented in the figure are the result of mixed-effects analysis, with Geisser-Greenhouse correction. Significance at individual points was determined by correction for multiple testing using false discovery rate (Benjamini and Hochberg). **(G)** MRI calculated total fat mass across study, normalized to pre-tumor baseline fat mass. Error bars are SEM, statistical analysis is as described above. **(H)** MRI calculated total lean mass across study, normalized to pre-tumor baseline lean mass. Error bars are SEM, statistical analysis is as described above. *$p<0.05$ by student's t test n= 5 vehicle, 4 tumor-bearing 7-week-old male 129S2/SvPasCrl mice for all data except survival curve.

Figure 2: Lung cancer-associated inflammation. (A) Heat map of 29 cytokines profiled in the serum of vehicle or tumor-bearing mice. Features are sorted by the highest average of the tumor samples, from top to bottom. Values are the

concentration, row normalized for each feature, then log2 transformed. Red = high expression, Blue = low expression. **(B)** Bar graph of cytokines commonly associated with muscle wasting and/or cancer cachexia. Individual points represent individual animals. Boxes represent the inner quartile and whiskers represent the minimum and maximum values. **(C)** Bar graph of cytokines significantly upregulated in tumor bearing animals. Individual points represent individual animals. Boxes represent the inner quartile and whiskers represent the minimum and maximum values. *$p<0.05$ in multiple t test with Holm-Sidak multiple testing correction. n= 5 vehicle, 4 tumor-bearing 7-week-old male 129S2/SvPasCrl mice.

Figure 3: Lung cancer-associated muscle loss. (A) Representative images of vehicle (left two images) and tumor-bearing (right two images) tibialis anterior (TA) muscle cross sections. Immunofluorescent staining for Laminin (myofiber membranes, white) and DAPI (nuclei, blue). **(B)** Quantification of minimum feret diameters of myofibers from tumor-bearing and vehicle mice. Feret diameters were binned to a histogram and fit with a non-linear regression (gaussian, least squares regression). Myofibers of tumor-bearing animals were significantly smaller than vehicle; $p=0.0142$. **(C)** Wet weight of TA muscle from vehicle and tumor-bearing animals. Individual points represent individual animals. Boxes represent the inner quartile and whiskers represent the minimum and maximum values. **(D)** Wet weight of gastrocnemius (GR) muscle from vehicle and tumor-bearing animals. Individual points represent individual animals. Boxes represent the inner quartile and whiskers represent the minimum and maximum values. **(E)** Quantification of Pax7 positive cells per millimeter squared in TA cross sections of vehicle or tumor-bearing animals. Individual points represent individual animals. Boxes represent the inner quartile and whiskers represent the minimum and maximum values. **(F)** Quantification of centrally located nuclei per myofiber in TA cross sections. Individual points represent individual animals. Boxes represent the inner quartile and whiskers represent the minimum and maximum values. **(G)** Heat map depicting 16 transcripts assessed by qPCR in

gastrocnemius muscle of vehicle or tumor-bearing animals. Transcripts are sorted by highest expression average of tumor sample from top to bottom. Orange = high expression, Blue = low expression. *P<0.05 by student's t test n= 5, 7-week-old male 129S2/SvPasCrl mice for each group.

Figure 4: Tumor cell number titration modulates survival time. (A) Survival curve for mice injected with vehicle or a range of tumor cells (300,000, 1 million, or 3 million). **(B)** Table depicting the median survival for each group. **(C)** Total lung weight (all lobes) in milligrams for each group. Individual points represent individual animals. Boxes represent the inner quartile and whiskers represent the minimum and maximum values. *p<0.05 student's t test. n= 5, vehicle; 4, 3-million; 5, 1-million; 3, 300,000 7-week-old male 129S2/SvPasCrl mice. **(D)** Representative images of lungs from vehicle, 300,000 cells and 3 million cells groups. Ruler reference is in centimeters.

Figure 5: Tumor-bearing mice exhibit progressive tissue loss regardless of initial transplanted cell number. (A) Total mouse weight across study, normalized to pre-tumor baseline weight. Error bars are SEM, statistical analysis is as described in 1F. **(B)** MRI calculated total fat mass across study, normalized to pre-tumor baseline fat mass. Error bars are SEM, statistical analysis is as described in 1F. **(C)** MRI calculated total lean mass across study, normalized to pre-tumor baseline lean mass. Error bars are SEM, statistical analysis is as described in 1F. **(D)** TA weight in milligrams for each group in study. Individual points represent individual animals. Boxes represent the inner quartile and whiskers represent the minimum and maximum values. **(E)** Quantification of minimum feret diameters from muscles of tumor-bearing (1 million cells or 300,000 cells) and vehicle-treated mice. Feret diameters were binned to a histogram and fit with a non-linear regression (gaussian, least squares regression). Myofibers from tumor-bearing mice were smaller, p values calculated by extra sun-of-squares F test. 1 million vs. vehicle (left, p= 0.0523),

373 300,000 vs. vehicle (right, $p<0.0001$). n= 5, vehicle; 4, 3-million; 5, 1-million; 3,
374 300,000 7-week-old male 129S2/SvPasCrl mice.

375

376 **Table 1: Metastatic characteristics of 393P lung cancer-associated wasting**
377 **model.** Percentage of animals bearing nodular tumors visible with the naked eye
378 during necropsy and qualitative assessment of necropsied animals showing
379 metastases in the thorax, lower back, and upper hindlimb regions.

380

381

METHODS

Animals

Mice were bred and housed according to NIH guidelines for the ethical treatment of animals in a pathogen-free facility at the Mayo Clinic (Rochester, MN campus). Mayo Clinic's Institutional Animal Care and Use Committee (IACUC) approved all animal protocols. For 393P-induced CAW model, 150 uL 393P cells (containing 3×10^6, 1×10^6, or 3×10^5 cells depending on group), or an equal volume of PBS (Gibco, 14190-144) (control) was injected via tail vein into 7-week-old male 129S2/SvPasCrl mice (Jackson Laboratories, Bar Harbor, ME). Development of cachexia was monitored twice weekly by body weight, fat, and lean mass. Mice were euthanized when endpoint criteria (weight loss greater than or equal to 20% of body weight, inability to ambulate, inability to reach food and/or water, tumors greater than or equal to 10% of body weight, tumors that have ulcerated, a body condition score of 1 or less using the IACUC approved scoring system) was reached. Blood serum, heart muscle, lungs, tibialis anterior (TA), gastrocnemius (GR) and epididymal fat pad were collected immediately for analyses. Exact n for each experiment included in the figure legends.

Animal imaging

Body weight, lean mass, and fat mass were measured twice weekly until endpoint. A baseline measurement was taken prior to start of study. Body composition was measured using magnetic resonance imaging (EchoMRI-100/130) system, EchoMRI, Houston, TX, USA).

Cell culture

393P cells were grown on tissue culture treated dishes in growth media consisting of DMEM media (Gibco #11995-065, lot 2051518) supplemented with 10% fetal bovine serum (Gibco #10099131, lot 2017488) and antibiotics. Cells were validated by IDEXX analytics and confirmed to be a pure culture and

murine in origin. Cells were removed from plate with TrypLE (Gibco, 12604-013), counted, and resuspended in PBS prior to injection.

Immunostaining

Left TA whole muscle was prepared for O.C.T embedding and cryosectioned. Tissue sections (8-10um) were post-fixed in 4% paraformaldehyde for 5 minutes at room temperature prior to immunostaining. Once fixed, isolated tissue sections were permeabilized with 0.5% Triton-X100 in PBS, followed by blocking with 3% BSA in PBS. Primary antibody incubations occurred at RT for 90 minutes or overnight in 4 degrees, and secondary antibody incubations followed at RT for 45 minutes in 3% BSA in PBS. The following antibodies were used in this study: Laminin (Sigma 4HB-2) and Pax7 (developmental hybridoma bank). Secondary antibodies were all Alexa fluorescent conjugates (488, 555, or 647) from Invitrogen or Jackson ImmunoResearch. Stained tissue sections were imaged on a (Nikon Eclipse Ti-U camera and microscope system). Acquired images were analyzed for myofiber feret diameters using myovison and manual colocalization quantification using ImageJ.

Cytokine Studies

Blood serum was collected from mice at endpoint. The MD31 cytokine panel was performed by Eve Technologies (Eve Technologies, Calgary, AB Canada) and samples were prepared as recommended by Eve Technologies. All samples were run in technical duplicate.

Q-PCR

Total gastrocnemius RNA was isolated, purified, and DNase I treated using Trizol and purified on RNeasy Mini kit columns (Qiagen, Mississauga, ON, Canada). RNA was quantified using a NanoDrop Spectrophotometer (ThermoScientific, Wilmington, DE, USA). Two ug of total RNA was reverse transcribed with primers using the High-Capacity cDNA Reverse Transcription Kit (Life Technologies, Carlsbad, CA, USA). QPCR was performed on a ViiA7

Quantitative PCR System (Applied Biosystems by Life Technologies, Austin, TX, USA). All samples were run in technical triplicate. Standard delta delta CT analysis was used post PCR. Primer sequences are available upon request.

Lung, Heart and TA Histopathology

At endpoint lung, heart and right TA whole muscle were fixed in 4% paraformaldehyde. After 24 hours, tissue was moved to 70% ethanol. Tissue was embedded in paraffin and tissue sections (6 um) were incubated at 37 degrees for 60 minutes prior to staining with hematoxylin and eosin (H&E). Stained tissue sections were analyzed by GEMpath Inc. (Dr. Brad Bolon, Longmont, CO) and imaged on a Nikon Eclipse Ts2 microscope. Samples could be segregated with 100% reliability at using both the naked eye and the microscope.

Statistics

Data are represented as the mean ± SD using GraphPad Prism (GraphPad Software, San Diego, CA) unless noted otherwise in the figure legends. Quantification of muscle cross sections using minimum feret diameter measurements was analyzed by non-linear regression (least squares method) and compared between conditions using an extra-sum-of-squares F test. All other comparisons between groups were performed using unpaired two-tailed student's t tests or mixed-effects analysis, as noted in figure legends. For all analyses, a $p<0.05$ was considered significant (denoted with *)

Data availability

Datasets generated during the current study are available from the corresponding author upon request.

REFERENCES

1. Zhu, R., et al., *Updates on the pathogenesis of advanced lung cancer-induced cachexia.* Thoracic cancer, 2019. **10**(1): p. 8-16.
2. Baracos, V.E., et al., *Body composition in patients with non-small cell lung cancer: a contemporary view of cancer cachexia with the use of computed tomography image analysis.* Am J Clin Nutr, 2010. **91**(4): p. 1133S-1137S.
3. Porporato, P.E., *Understanding cachexia as a cancer metabolism syndrome.* Oncogenesis, 2016. **5**: p. e200.
4. Jatoi, A., et al., *A placebo-controlled, double-blind trial of infliximab for cancer-associated weight loss in elderly and/or poor performance non-small cell lung cancer patients (N01C9).* Lung Cancer, 2010. **68**(2): p. 234-9.
5. Pettersen, K., et al., *Cancer cachexia associates with a systemic autophagy-inducing activity mimicked by cancer cell-derived IL-6 trans-signaling.* Sci Rep, 2017. **7**(1): p. 2046.
6. Yuan, L., et al., *Muscle-specific E3 ubiquitin ligases are involved in muscle atrophy of cancer cachexia: an in vitro and in vivo study.* Oncol Rep, 2015. **33**(5): p. 2261-8.
7. Baracos, V.E., et al., *Activation of the ATP-ubiquitin-proteasome pathway in skeletal muscle of cachectic rats bearing a hepatoma.* Am J Physiol, 1995. **268**(5 Pt 1): p. E996-1006.
8. Kellar, A., C. Egan, and D. Morris, *Preclinical Murine Models for Lung Cancer: Clinical Trial Applications.* Biomed Res Int, 2015. **2015**: p. 621324.
9. Tanaka, Y., et al., *Experimental cancer cachexia induced by transplantable colon 26 adenocarcinoma in mice.* Cancer Res, 1990. **50**(8): p. 2290-5.
10. Aulino, P., et al., *Molecular, cellular and physiological characterization of the cancer cachexia-inducing C26 colon carcinoma in mouse.* BMC Cancer, 2010. **10**: p. 363.
11. Lewis, B.C., D.S. Klimstra, and H.E. Varmus, *The c-myc and PyMT oncogenes induce different tumor types in a somatic mouse model for pancreatic cancer.* Genes & development, 2003. **17**(24): p. 3127-3138.
12. Shukla, S.K., et al., *Silibinin-mediated metabolic reprogramming attenuates pancreatic cancer-induced cachexia and tumor growth.* Oncotarget, 2015. **6**(38): p. 41146.
13. Talbert, E.E., et al., *Modeling Human Cancer-induced Cachexia.* Cell Rep, 2019. **28**(6): p. 1612-1622 e4.
14. Frese, K.K. and D.A. Tuveson, *Maximizing mouse cancer models.* Nature Reviews Cancer, 2007. **7**(9): p. 654.
15. Goncalves, M.D., et al., *Fenofibrate prevents skeletal muscle loss in mice with lung cancer.* Proceedings of the National Academy of Sciences, 2018. **115**(4): p. E743-E752.

16. Fujiwara, T., et al., *Therapeutic Effect of a Retroviral Wild-Type p53 Expression Vector in an Orthotopic Lung Cancer Model.* JNCI: Journal of the National Cancer Institute, 1994. **86**(19): p. 1458-1462.
17. Howard, R.B., et al., *Characterization of a highly metastatic, orthotopic lung cancer model in the nude rat.* Clinical & experimental metastasis, 1999. **17**(2): p. 157-162.
18. DuPage, M., A.L. Dooley, and T. Jacks, *Conditional mouse lung cancer models using adenoviral or lentiviral delivery of Cre recombinase.* Nat Protoc, 2009. **4**(7): p. 1064-72.
19. Doles, J., et al., *Suppression of Rev3, the catalytic subunit of Pol{zeta}, sensitizes drug-resistant lung tumors to chemotherapy.* Proc Natl Acad Sci U S A, 2010. **107**(48): p. 20786-91.
20. Ma, J.F., et al., *STAT3 promotes IFNγ/TNFα-induced muscle wasting in an NF-κB-dependent and IL-6-independent manner.* EMBO Mol Med, 2017. **9**(5): p. 622-637.
21. Zimmers, T.A., M.L. Fishel, and A. Bonetto, *STAT3 in the systemic inflammation of cancer cachexia.* Semin Cell Dev Biol, 2016. **54**: p. 28-41.
22. Hogan, K.A., et al., *Tumor-derived cytokines impair myogenesis and alter the skeletal muscle immune microenvironment.* Cytokine, 2017.
23. Magee, P., S. Pearson, and J. Allen, *The omega-3 fatty acid, eicosapentaenoic acid (EPA), prevents the damaging effects of tumour necrosis factor (TNF)-alpha during murine skeletal muscle cell differentiation.* Lipids Health Dis, 2008. **7**: p. 24.
24. Wen, Y., et al., *MyoVision: software for automated high-content analysis of skeletal muscle immunohistochemistry.* J Appl Physiol (1985), 2018. **124**(1): p. 40-51.
25. Muir, A., L.V. Danai, and M.G. Vander Heiden, *Microenvironmental regulation of cancer cell metabolism: implications for experimental design and translational studies.* Dis Model Mech, 2018. **11**(8).
26. Yanagihara, K., et al., *Development and characterization of a cancer cachexia model employing a rare human duodenal neuroendocrine carcinoma-originating cell line.* Oncotarget, 2019. **10**(25): p. 2435.
27. Erstad, D.J., et al., *Orthotopic and heterotopic murine models of pancreatic cancer and their different responses to FOLFIRINOX chemotherapy.* Disease models & mechanisms, 2018. **11**(7): p. dmm034793.
28. Horikawa, N., et al., *Expression of vascular endothelial growth factor in ovarian cancer inhibits tumor immunity through the accumulation of myeloid-derived suppressor cells.* Clinical Cancer Research, 2017. **23**(2): p. 587-599.
29. Tachibana, K., et al., *IL-17 and VEGF are increased and correlated to systemic inflammation, immune suppression, and malnutrition in patients with breast cancer.* European Journal of Inflammation, 2017. **15**(3): p. 219-228.

549 30. Gelin, J., et al., *Role of endogenous tumor necrosis factor alpha and*
550 *interleukin 1 for experimental tumor growth and the development of cancer*
551 *cachexia.* Cancer Res, 1991. **51**(1): p. 415-21.
552 31. He, W.A., et al., *NF-κB-mediated Pax7 dysregulation in the muscle*
553 *microenvironment promotes cancer cachexia.* J Clin Invest, 2013.
554 **123**(11): p. 4821-35.
555 32. Pfeifer, A. and I.M. Verma, *Gene therapy: promises and problems.* Annual
556 review of genomics and human genetics, 2001. **2**(1): p. 177-211.
557 33. White, R.B., et al., *Dynamics of muscle fibre growth during postnatal*
558 *mouse development.* BMC developmental biology, 2010. **10**(1): p. 21.
559 34. Aoki, T., et al., *Evolution of peripheral lung adenocarcinomas: CT findings*
560 *correlated with histology and tumor doubling time.* American journal of
561 roentgenology, 2000. **174**(3): p. 763-768.
562 35. Zhang, Y., et al., *Frequency of driver mutations in lung adenocarcinoma*
563 *from female never-smokers varies with histologic subtypes and age at*
564 *diagnosis.* Clinical cancer research, 2012. **18**(7): p. 1947-1953.
565 36. Fearon, K., et al., *Definition and classification of cancer cachexia: an*
566 *international consensus.* Lancet Oncol, 2011. **12**(5): p. 489-95.
567

Figure 1

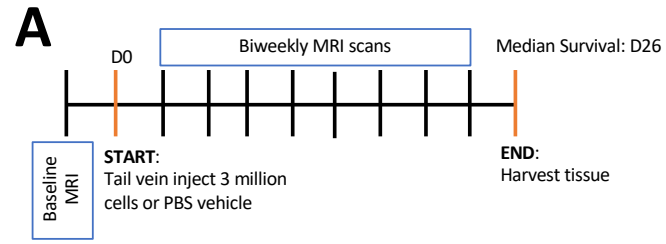

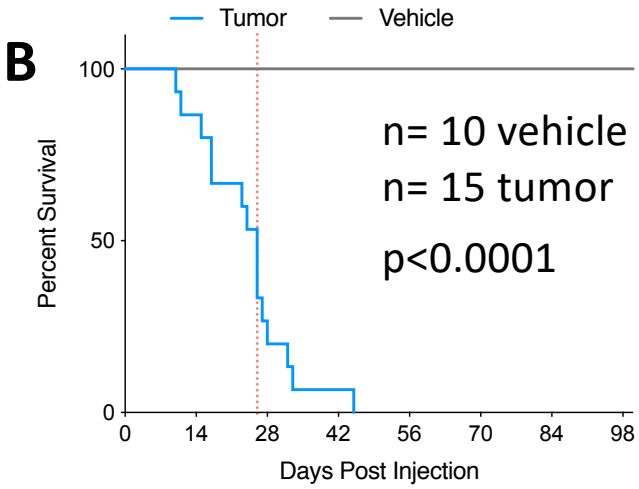

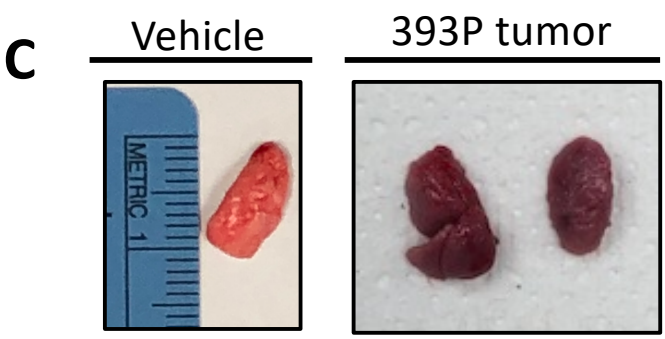

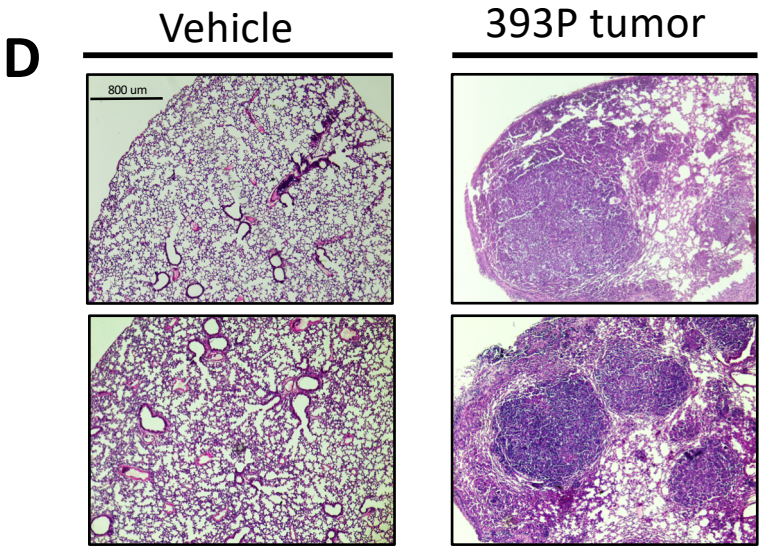

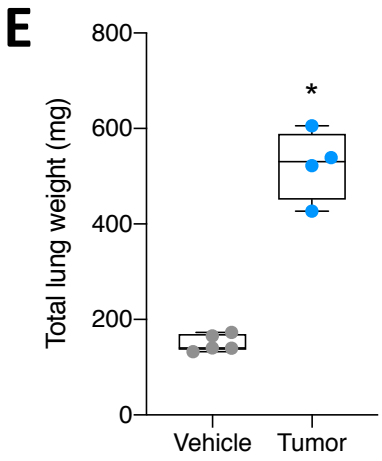

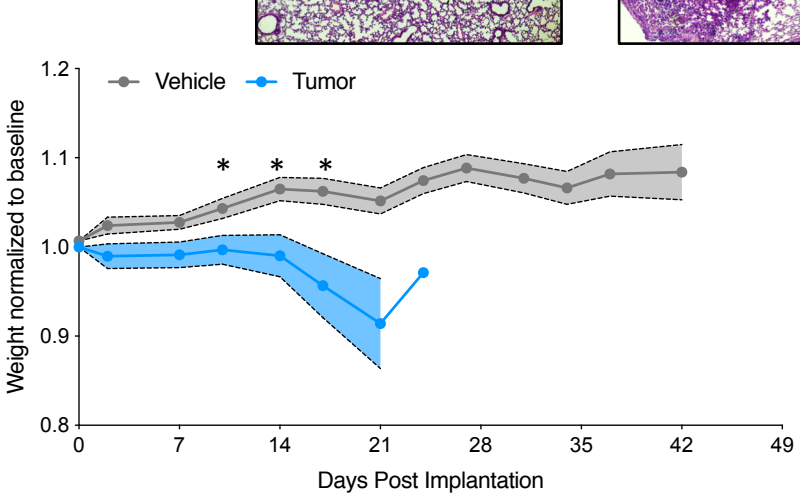

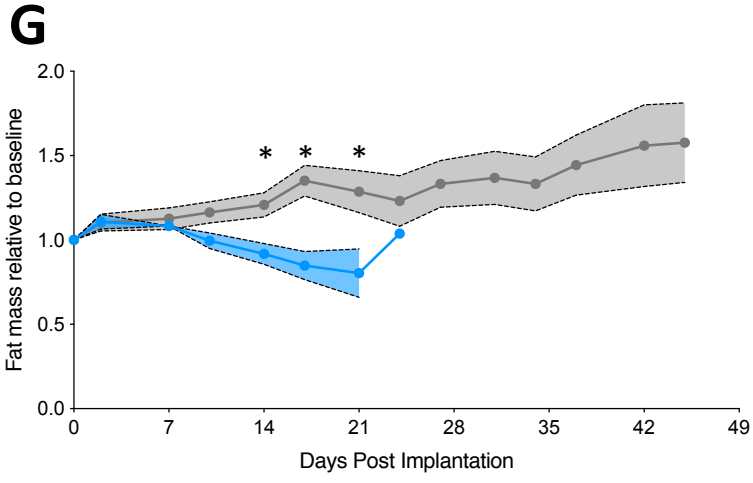

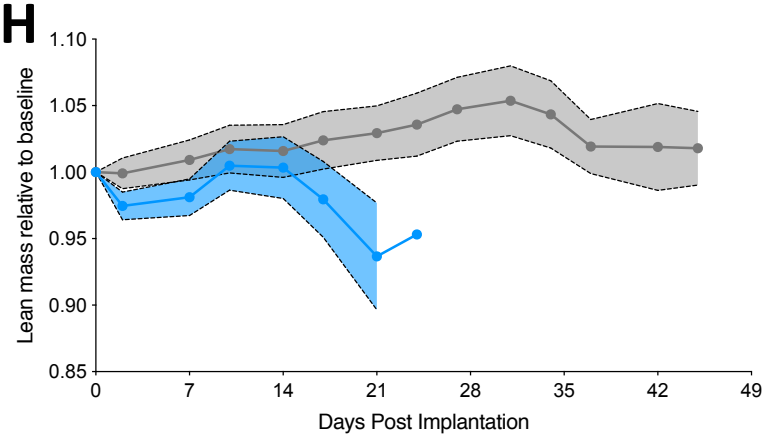

Figure 2

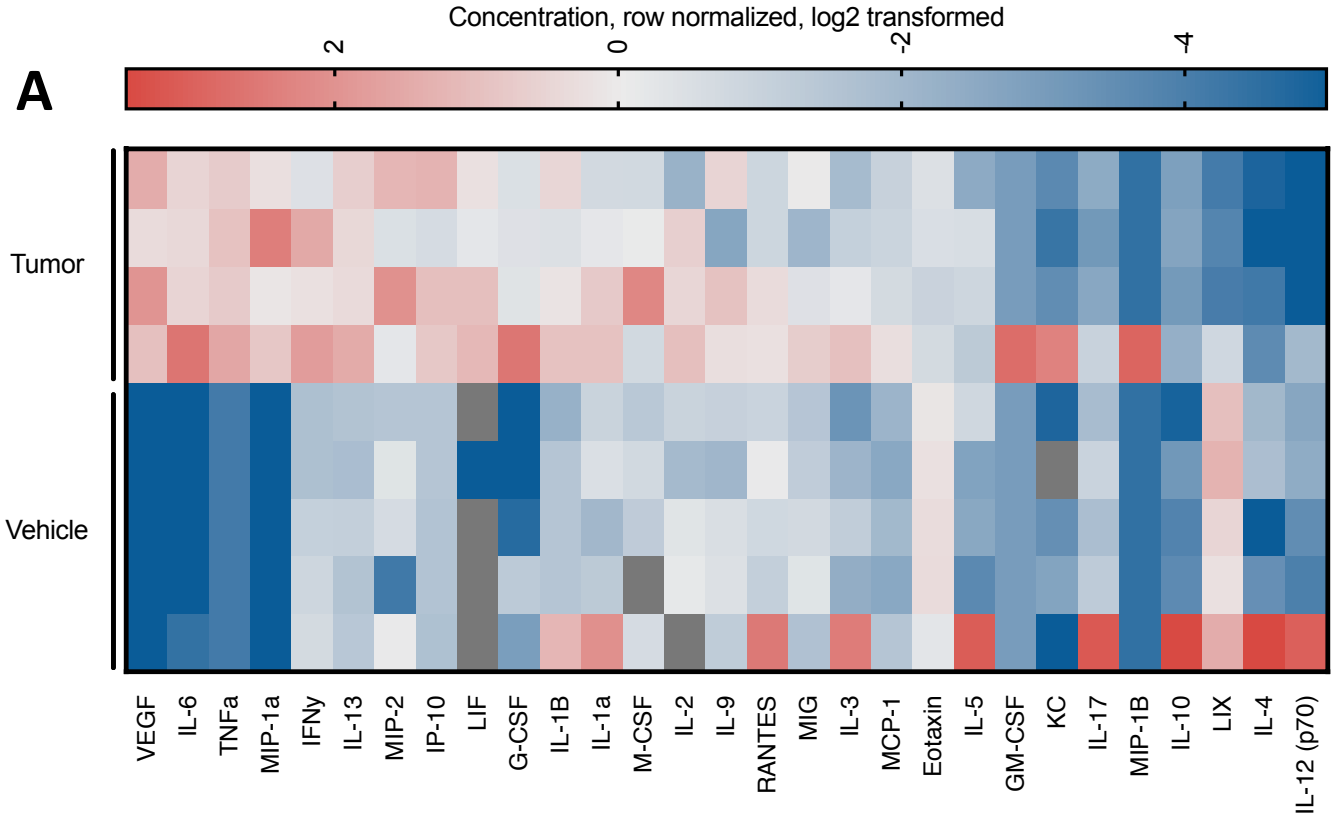

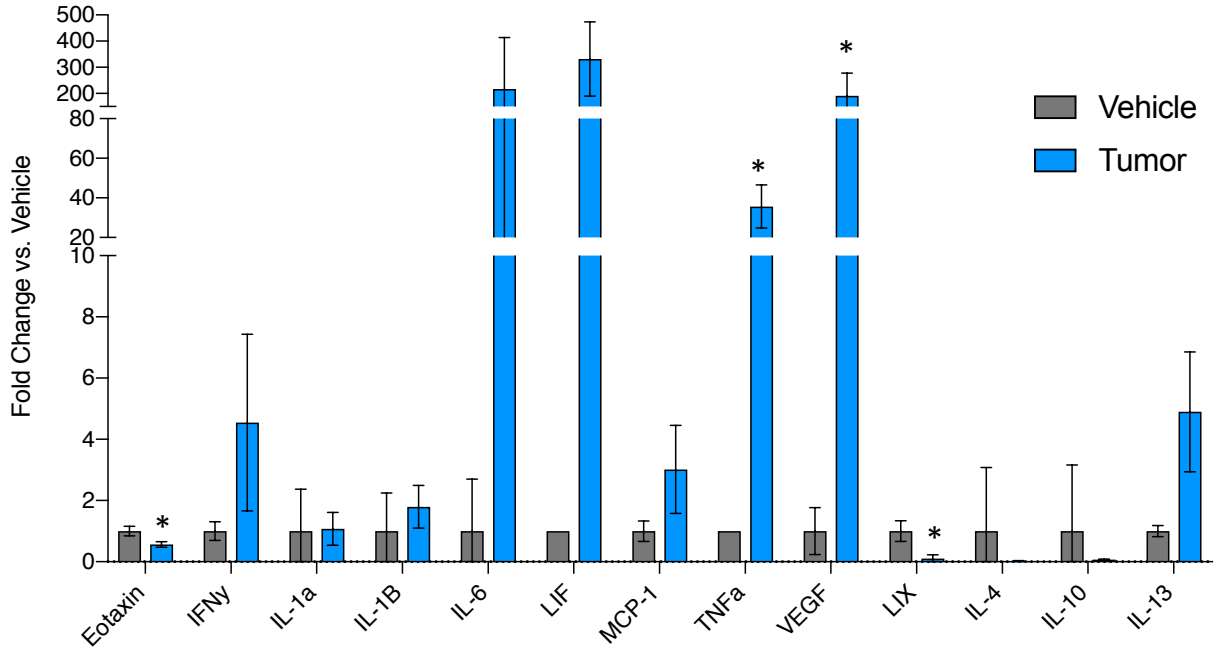

Figure 3

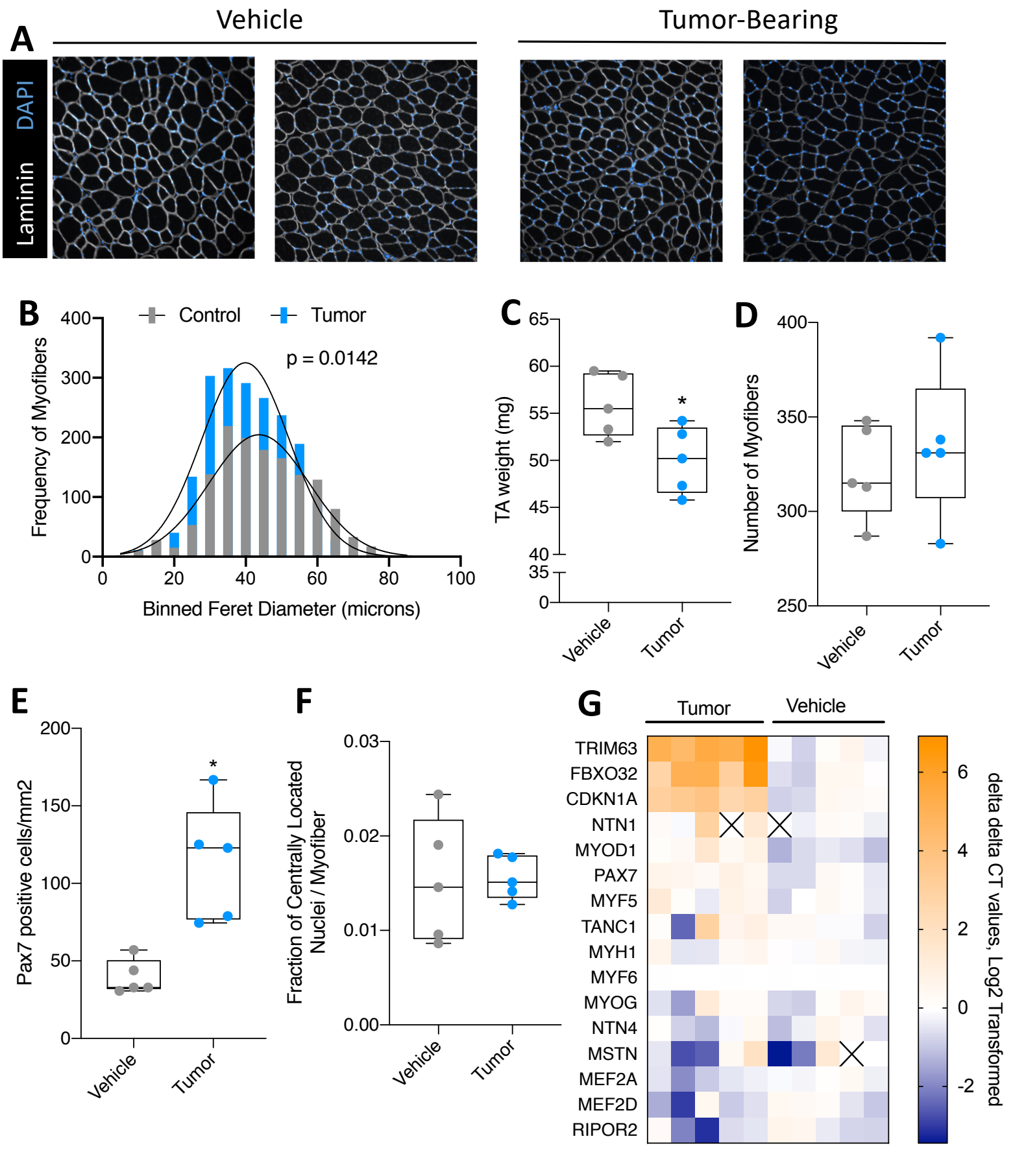

Figure 4

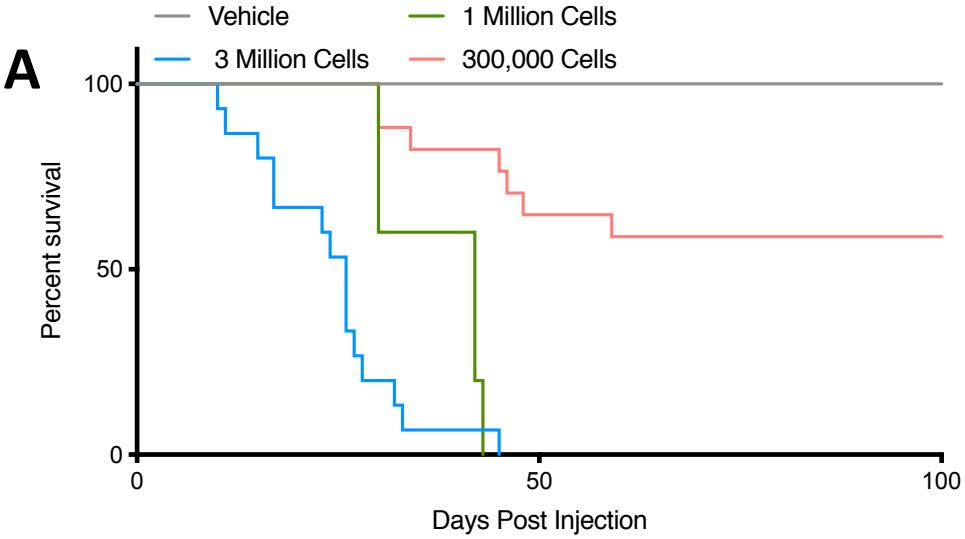

B

Cells Implanted	Median Survival (Days)
Vehicle	No Deaths
3 Million Cells	26
1 Million Cells	42
300,000 Cells	107

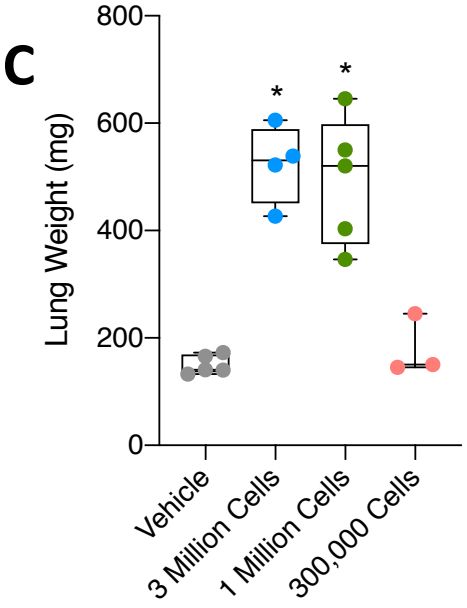

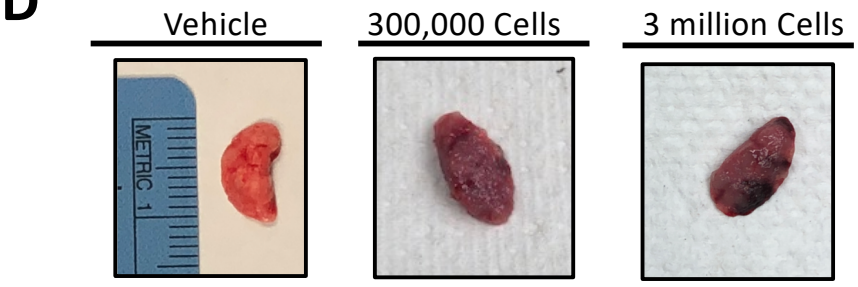

Figure 5

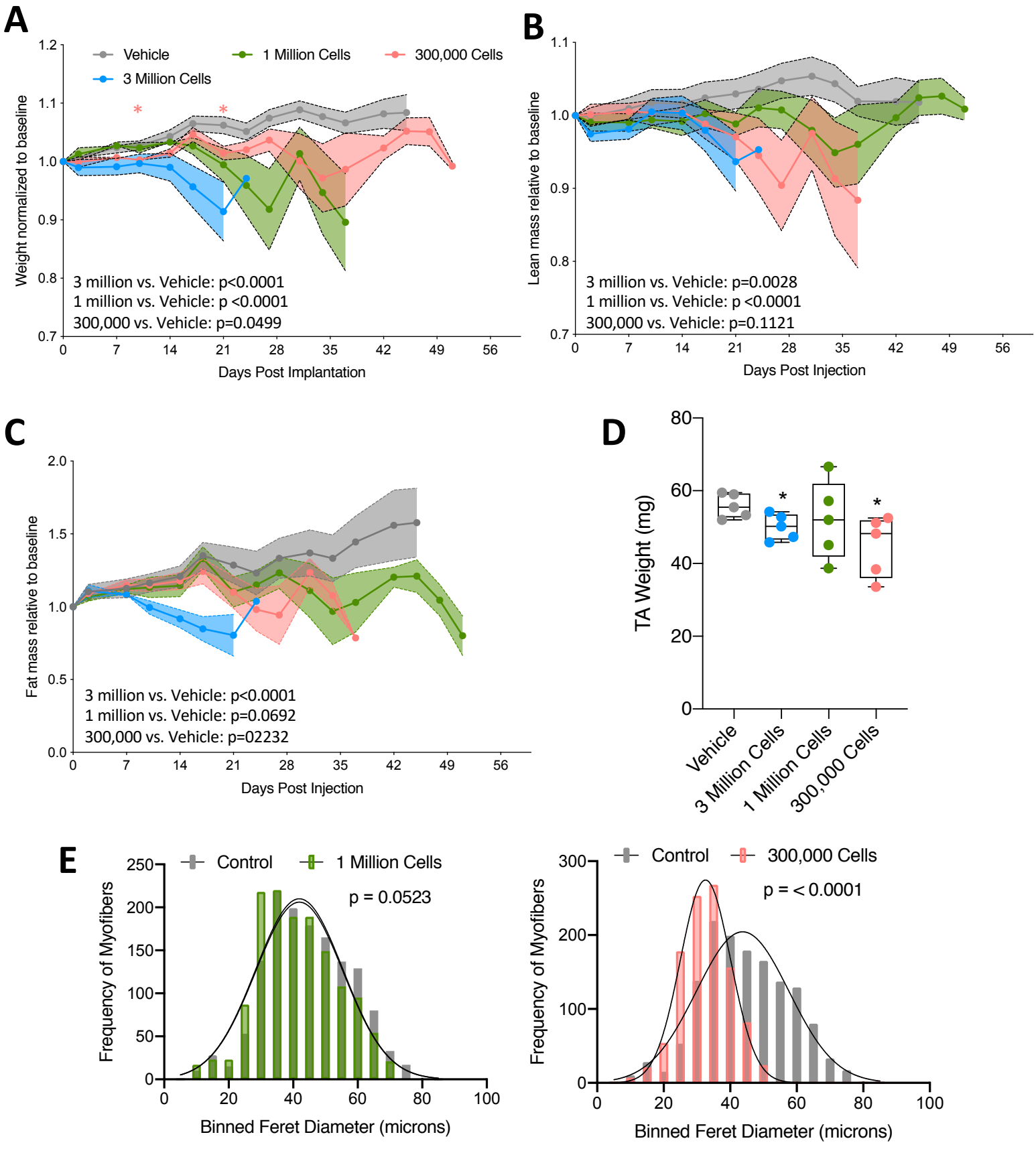

Table 1

Group	% with Lung Tumor	% with Other Tumors	% with Metastasis in Thoracic Cavity
3,000,000 (n=15)	93	33 lower back 10 hindlimb	73
1,000,000 (n=5)	100	100	100
300,000 (n=15)	67	33 lower back	53
Vehicle (n=10)	0	0	0